

PLANETS ON THE EDGE

FRANCESCA VALSECCHI^{1,2}, FREDERIC A. RASIO^{1,2}¹Center for Interdisciplinary Exploration and Research in Astrophysics (CIERA) and²Department of Physics and Astronomy, Northwestern University, 2145 Sheridan Road, Evanston, IL 60208, USA.*Draft version February 28, 2024*

ABSTRACT

Hot Jupiters formed through circularization of high-eccentricity orbits should be found at orbital separations a exceeding *twice* that of their Roche limit a_R . Nevertheless, about a dozen giant planets have now been found well within this limit ($a_R < a < 2a_R$), with one coming as close as $1.2a_R$. In this Letter, we show that orbital decay (starting beyond $2a_R$) driven by tidal dissipation in the star can naturally explain these objects. For a few systems (WASP-4 and 19), this explanation requires the linear reduction in convective tidal dissipation proposed originally by Zahn (1966, 1989) and verified by recent numerical simulations (Penev et al. 2007), but rules out the quadratic prescription proposed by Goldreich & Nicholson (1977). Additionally, we find that WASP-19-like systems could potentially provide direct empirical constraints on tidal dissipation, as we could soon be able to measure their orbital decay through high precision transit timing measurements.

Subject headings: Planetary Systems: planet-star interactions—planets and satellites: gaseous planets—stars: evolution—stars: general—(stars:) planetary systems

1. INTRODUCTION

Almost 200 of the known transiting exoplanets are giant planets with orbital periods less than 10 days. These so-called hot Jupiters were most likely formed farther out at several AUs, but the debate continues on whether their tight orbits are the result of quasi-circular *disk migration* or *high-eccentricity migration*. The first scenario involves slow orbital decay in a protoplanetary disk (Goldreich & Tremaine 1980; Lin et al. 1996; Ward 1997; Murray et al. 1998), while the second involves tidal circularization of an orbit made extremely eccentric by gravitational interaction with companion stars, or between several planets (Rasio & Ford 1996; Wu & Murray 2003; Fabrycky & Tremaine 2007; Nagasawa et al. 2008; Wu & Lithwick 2011; Naoz et al. 2011; Plavchan & Bilinski 2013). In this letter, we focus on the hot Jupiters close to their Roche limits and show that they provide an important test for giant planet formation theories. In particular, this population provides constraints on the efficiency of convective damping of equilibrium tides (Zahn 1966, 1989; Goldreich & Nicholson 1977; see also Sasselov 2003).

In the disk-migration scenario, gas giants should be naturally found distributed in orbital separations, all the way down to the Roche limit a_R . Instead, in any high-eccentricity migration scenario, Ford & Rasio (2006) pointed out that tidal circularization would lead to an inner edge at $2a_R$. While the great majority of systems are indeed observed to lie beyond $2a_R$ (e.g., Matsumura et al. 2010 and Fig. 1 here), several hot Jupiters have now been discovered inside this limit. In a recent paper (Valsecchi & Rasio 2014, hereafter VR14), we targeted giant planets in misaligned systems (where the stellar spin and orbital angular momentum are misaligned on the plane of the sky) and we showed that their properties could be naturally explained

through high-eccentricity migration. Hot Jupiters can then be formed with a broad distribution of misalignments λ and in orbits with a high eccentricity, which is quickly dissipated by planetary tides (Jackson et al. 2008; Matsumura et al. 2010). Subsequently, stellar tides, magnetic braking, and stellar evolution lead to the observed distribution of λ found around stars of different temperatures (Winn et al. 2010; Albrecht et al. 2012). Here we consider the known hot Jupiters close to tidal disruption and investigate the possibility that these same physical mechanisms are responsible for bringing them inward from *beyond* $2a_R$. As the tides exerted on the star by the planet are expected to be too weak to keep up with the spin-down driven by magnetic braking (Barker & Ogilvie 2009), the resulting dissipation in the slowly rotating host star drives further orbital decay. With future measurements of the shift in transit times (e.g., Sasselov 2003; Birkby et al. 2014), the orbital decay rate could be determined. This, in turn, would provide important constraints for both tidal dissipation and hot Jupiter formation theories. In contrast to previous studies on these objects (e.g., Sasselov 2003; Gillon et al. 2014; Birkby et al. 2014), we use detailed stellar models and compute the orbital evolution of hot Jupiters by integrating the equations describing the coupled evolution of the orbital elements and stellar spin (VR14).

This paper is organized as follows. We describe our hot Jupiter sample in § 2 and explain how we model each host star in § 3. In § 4 we summarize the physical mechanisms included in our orbital evolution calculations and we emphasize the tidal prescriptions considered. We present our results in § 5 and conclude in § 6.

In what follows M_* , R_* , T_{eff} , Fe/H (or Z), λ (Θ_*), and $v_{\text{rot}} \sin i_*$ indicate the stellar mass, radius, effective temperature, metallicity, sky-projected (true) misalignment, and rotational velocity, respectively. The angles λ and Θ_* are related via $\cos \Theta_* = \sin i_* \cos \lambda \sin i_o + \cos i_* \cos i_o$ (Fabrycky & Winn 2009). The angle between the stellar spin axis (the orbital angular momentum) and the line

of sight is i_* (i_o). The planetary mass (radius) is M_{pl} (R_{pl}). The stellar spin frequency and planetary orbital frequency are Ω_* and Ω_o , respectively. The orbital period (separation) is P_{orb} (a).

2. HOT JUPITERS WITHIN $2a_R$

The systems were queried from the NASA Exoplanet Archive on 20 February 2014. In Fig. 1 we show M_{pl}/M_* as a function of a/a_R for the full sample of exoplanets currently known (left) and for the systems considered here (right). We adopt Paczyński’s (1971) approximation $a_R = R_{\text{pl}}/(0.462q^{1/3})$, where $q = M_{\text{pl}}/M_* \ll 1$. The vertical dotted line marks the $a/a_R = 2$ limit, beyond which lie the great majority of systems. Here we focus on the hot Jupiters inside this limit where no additional bodies have been found (marked in grey, as such bodies could perturb the orbital evolution of the inner planet). We summarize their properties in Table 1.

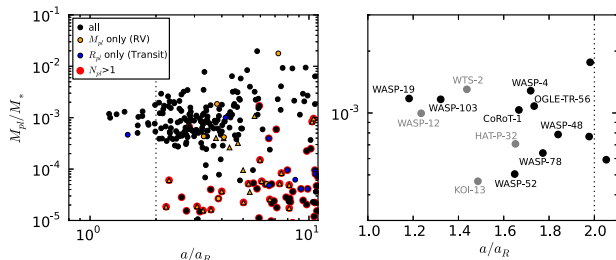


Figure 1. Ratio of planetary to stellar mass as a function of the orbital distance to Roche limit ratio. The vertical dotted line is at $a/a_R = 2$. Left: exoplanets for which P_{orb} , M_* , and M_{pl} or R_{pl} are known within the range of M_{pl}/M_* and a/a_R displayed. In black are the systems where P_{orb} , M_* , M_{pl} , and R_{pl} have been constrained. In blue (orange) are the systems where only R_{pl} (M_{pl}) is known through transit [radial velocity (RV)] measurements. Like Matsumura et al. (2010), when R_{pl} is unknown, we assume a Neptune (Jupiter) radius if $M_{\text{pl}} < 0.1 M_J$ ($> 0.1 M_J$); when M_{pl} is unknown we assume a Neptune (Jupiter) mass if $R_{\text{pl}} < 0.35 R_J$ ($> 0.35 R_J$). The orange triangles denote lower limits (only $M_{\text{pl}} \sin i_o$ is known), while the red circles denote systems with multiple planets. Right: systems considered in this work (black) and systems where additional bodies have been found (in grey; Santerne et al. 2012; Bechter et al. 2013; Knutson et al. 2013; Birkby et al. 2014). The properties of the systems considered here have been updated from exoplanet.eu and we also include the recently discovered WTS-2 (Birkby et al. 2014). The size of the data points does not represent the uncertainties.

3. STELLAR MODELS

The host star models are shown in Fig. 2 and are chosen from the grid of evolutionary tracks described in VR14 (computed with MESA; Paxton et al. 2011, 2013) as follows. To be within the 1σ uncertainties in M_* and Fe/H , while still close to the mean observed values, OGLE-TR-56, WASP-4, 19, and 48’s models are chosen randomly among those whose M_* (Fe/H) are within $0.04 M_\odot$ (0.05) from the observed mean values at some point during the stellar evolution. The same procedure is applied to CoRoT-1 and WASP-103, but requiring the limit on M_* (Fe/H) to be $0.03 M_\odot$ (0.05). The age of WASP-52 varies by several Gyr, depending on its properties. Hébrard et al. (2013) report a lower limit of 0.5 Gyr from lithium abundance and quote a gyrochronological age of $0.4^{+0.3}_{-0.2}$ Gyr derived from the observed $v_{\text{rot}} \sin i_*$ (Hébrard et al. 2013 and references therein). However, i_*

is not known. To see some degree of orbital evolution we take the model that reaches the oldest age within the 1σ uncertainties in M_* and Fe/H . This model spans a range $\simeq 1.5 - 7$ Gyr. Finally, WASP-78 is not in VR14’s catalogue, and we evolve a star with the observed mean M_* and Z . The observed R_* and T_{eff} can be matched only within 2σ . The agreement could be improved by varying some of the physics entering the stellar modeling (e.g., the mixing length parameter, which is usually varied between 1–2 in the literature, see Paxton et al. 2011, 2013). However, we choose not to introduce additional free parameters and therefore apply the same physical assumptions to all systems.

4. ORBITAL EVOLUTION

The procedure and assumptions adopted in our calculations are explained in detail in VR14. Here we outline the main points for clarity and present the new tidal prescriptions considered. We study CoRoT-1 b, OGLE-TR-56 b, WASP-4, 19, 48, 52, and 103 b’s evolutionary past, by scanning the initial [at the stellar Zero Age Main Sequence (ZAMS)] parameter space made of P_{orb} , Ω_*/Ω_o , and Θ_* (when measured). We then integrate the equations describing the coupled evolution of a , Ω_* , and Θ_* , due to stellar tides, wind mass loss, magnetic braking, and the evolution of the host star (§ 3). All orbits are consistent with circular and we assume that damping of the eccentricity occurred quickly through dissipation in the planet (this assumption is discussed in VR14). For all parameters described below, we adopt the same values used in VR14, unless stated otherwise.

For stellar wind mass loss and magnetic braking we proceed as in VR14, introducing the parameter γ_{MB} , which controls the strength of angular momentum loss via magnetic braking. For tides, we use the weak-friction approximation when there is no information about misalignment (and we then take $\Theta_* = 0$). Instead, for systems where the misalignment has been constrained, we include the effect of inertial wave dissipation (IWD) following Lai (2012), and consider a variety of initial Θ_* . When accounting for weak-friction tides *alone*, we consider both sub- and super-synchronous initial configurations ($\Omega_* < \Omega_o$ and $\Omega_* > \Omega_o$, respectively) and vary Ω_*/Ω_o between 0 and 100 in steps of 0.2. We halt the calculation if the star is spinning faster than break-up. Instead, when accounting for IWD, we consider initial Ω_*/Ω_o values only up to 0.9, according to the validity of the Lai (2012) prescription. Furthermore, we consider different values for the efficiency of IWD by varying the tidal quality factor Q'_{10} .

Thus far, we followed VR14, apart for enforcing the validity of the Lai’s (2012) recipe for tides (initial $\Omega_*/\Omega_o < 1$). Now we go one step further and vary the weak-friction tides prescription following Sasselov (2003). In VR14 we included the effects of both convective damping of the equilibrium tide and radiative damping of the dynamical tide and showed that, in the weak-friction regime, the former always dominates for typical hot Jupiter systems. For convective dissipation, we followed the mixing-length theory of convection and assumed that the oscillatory tidal distortion is dissipated by turbulent (eddy) viscosity. For high tidal forcing frequencies, the efficiency of angular momentum transport by the largest eddies is inhibited, and the exact form of this reduction

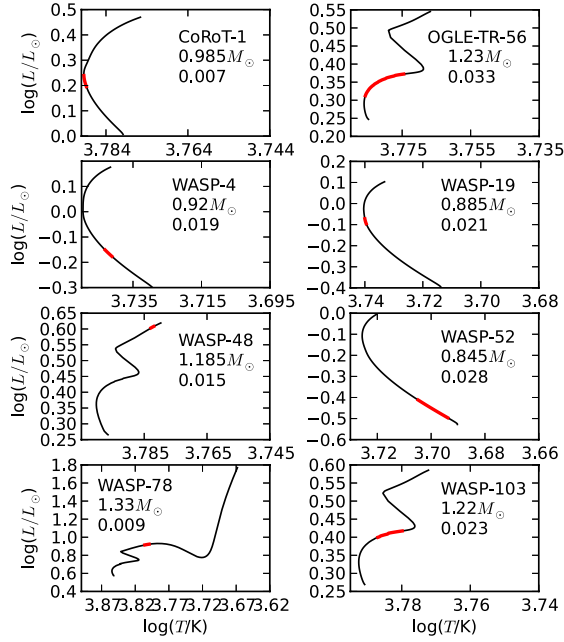


Figure 2. Hertzsprung-Russell (HR) diagrams for all systems. The numbers quoted in each panel are the stellar initial mass and metallicity Z . The red solid lines represent the models which match the observed Z , M_* , R_* , and $T_{\text{eff},*}$ within 1σ (Table 1), except for WASP-78 (where we can only match the observed R_* , and $T_{\text{eff},*}$ within 2σ ; see § 3).

is still under debate. Defining the reduction factor as

$$f_{*,\text{conv}} = \min \left[1, \left(\frac{P_{*,\text{tid}}}{2\tau_{*,\text{conv}}} \right)^s \right], \quad (1)$$

where $P_{*,\text{tid}}$ and $\tau_{*,\text{conv}}$ are the tidal forcing period and the convective turnover timescale (VR14 and references therein), two commonly used prescriptions are the linear one ($s = 1$) proposed by Zahn (1966, 1989) and supported by Penev et al.’s (2007) recent numerical simulations, and the quadratic one ($s = 2$) proposed by Goldreich & Nicholson (1977). Here we follow Sasselov (2003) and consider both $s = 1$ and $s = 2$ (hereafter the *Zahn* and *GN* prescription, respectively).

At each time-step during the calculation we check that the planet is within its Roche lobe (Paczynski 1971). We stop the evolution when the model’s M_* , R_* , $T_{\text{eff},*}$, $v_{\text{rot}} \sin i_*$, and Θ_* (if constrained) are within 1σ (2σ in R_* and $T_{\text{eff},*}$ for WASP-78) from the observed values and P_{orb} crosses the present value (Table 1).

5. RESULTS

Our numerical results are summarized in Table 2. The parameter T_{shift} , is the transit arrival time shift, which we computed following § 7.2 of Birkby et al. (2014) and our \dot{a} values. Here we follow Birkby et al. (2014) and assume 10 years of observations with a timing accuracy of 5 s (Gillon et al. 2009). However, note that orbital periods are routinely measured to less than 1 s with multiple observations (Jason Steffen, private communication). In Table 2, we therefore list the full range of T_{shift} values computed. We perform a first scan in initial orbital periods ($P_{\text{orb},\text{in}}$) with a coarse resolution, which we then increase during a second scan, if needed. In Table 2 we list the results with limited precision, just to give a sense for the possible initial orbital configurations.

Half of the systems considered are easily explained: CoRoT-1, OGLE-TR-56, WASP-48, and 103, according to our detailed modeling, started their orbital evolution from beyond $2a_R$, independent of the tidal prescription adopted (*Zahn* or *GN*). On the other hand, the evolutionary picture differs for WASP-4 and 19, where only the *Zahn* prescription is consistent with $a_{\text{in}} > 2a_R$. While for WASP-4 T_{shift} is lower than the 5 s limit considered by Birkby et al. (2014), it is 5–8 times this limit for WASP-19, according to *Zahn*. If detected, it could provide important constraints on tidal dissipation theory. Interestingly, WASP-19-like systems could also be used to constrain the efficiency of IWD. In fact, within the range of Q'_{10} values considered and given the resolution of our initial parameter space, this system can be explained by the *Zahn* (*GN*) prescription only if $Q'_{10} < 10^{10}$ ($Q'_{10} \geq 10^7$). Finally, WASP-52 and 78 are consistent with $a_{\text{in}} > 2a_R$ only for the longest $P_{\text{orb},\text{in}}$ considered. For WASP-52, a more precise determination of its age could provide constraints on the more likely migration scenario. Furthermore, within our initial parameter space, this system cannot be explained by the *GN* prescription. This is due to the upper limit imposed on the initial Ω_*/Ω_o . For WASP-78 the efficiency of tides is never reduced and both tidal prescriptions predict the same evolutionary picture. This system could still be used to constrain hot Jupiter formation theories from measurements of T_{shift} .

The ages constrained with our modeling (Table 2) agree with those reported in the literature (when available) for most systems. WASP-48’s age is uncertain and, even though we list the one derived by the lack of lithium and Ca H+K, we note that the rotation rate supports an age of $0.6^{+0.4}_{-0.2}$ Gyr. Alternatively, isochrones analysis yields an age of $3.0^{+1.0}_{-0.5}$ Gyr (Enoch et al. 2011 and references therein).

The parameter γ_{MB} is generally set to 0.1 and 1 for F- and G-dwarfs (Barker & Ogilvie 2009; Matsumura et al. 2010), respectively. We find solutions for nearly any of the γ_{MB} values considered for OGLE-TR-56, WASP-48, and 52, with both tidal prescriptions, and for WASP-4, and 103 with the *Zahn* prescription. Furthermore, the γ_{MB} range that explains WASP-78 ($\gamma_{\text{MB}} \leq 0.3$) and 103 ($\gamma_{\text{MB}} \leq 1$ and 0.2 for *Zahn* and *GN*, respectively) encloses the value 0.1 generally adopted for F-dwarfs. Instead, CoRoT-1, WASP-4, and 19, with G-dwarfs, all have $\gamma_{\text{MB}} < 1$. According to *Zahn* (*GN*), we find $\gamma_{\text{MB}} \leq 0.1$ (0.2) both for CoRoT-1 and WASP-19. On the other hand, for WASP-4, the *GN* prescription allows $\gamma_{\text{MB}} \leq 0.2$ (0.9) for $Q'_{10} = 10^6$ ($\geq 10^7$). This discrepancy and the fact that the *GN* prescription can not explain WASP-52 is due to the upper limit on the initial Ω_*/Ω_o considered here (0.9), as the Lai (2012) recipe for tides is strictly valid for sub-synchronous systems. In this regime, IWD affects only Ω_* and Θ_* , while it might affect a when $\Omega_* \geq \Omega_o$ (see VR14), but we do not account for this possibility. Since we find evolutionary solutions for initial Ω_*/Ω_o values up to 0.9, super-synchronous configurations would likely yield more solutions and higher γ_{MB} values. However, a different prescription for the evolution of a should then be adopted or a detailed study of the significance of IWD compared to the other physical mechanisms should be performed (VR14).

In Fig. 3 we show, as an example, the detailed evolution

of a WASP-4-like system according to *Zahn* (*GN*) in black (blue). This is an interesting system since only with the *Zahn* prescription could its orbit have begun beyond $2 a_R$.

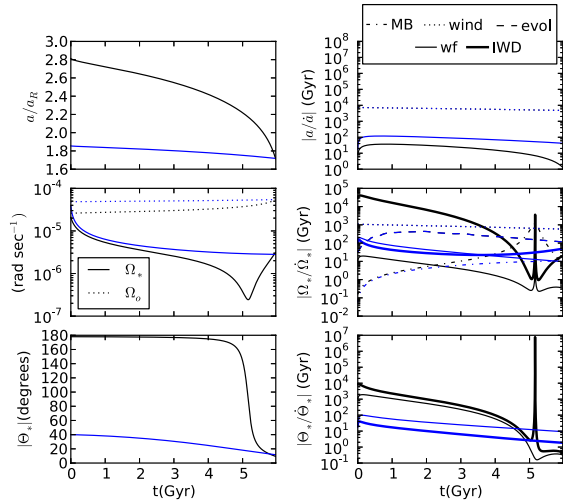


Figure 3. Detailed orbital evolution of a WASP-4-like system. Left: evolution of the orbital separation (top), stellar spin and orbital frequency (middle), and misalignment (bottom). Right: evolution of the timescales associated with the physical effects considered. Specifically, “wf” refers to tides in the weak friction approximation [Eqs. (1)–(3) in VR14], “evol” refers to changes in the stellar moment of inertia [Eqs. (10) in VR14], “IWD” refers to dissipation of inertial waves [the sum of the second and third terms on the right side of Eqs. (17) and (18) in VR14], “wind” refers to stellar wind mass loss [Eqs. (11)–(12) in VR14], and “MB” refers to magnetic braking [Eqs. (13) in VR14]. In black (blue) is the evolution according to *Zahn* (*GN*). For the *Zahn* (*GN*) example, the initial conditions are: $P_{\text{orb}} = 2.8$ d (1.5 d), $\Omega_*/\Omega_o = 0.8$ (0.8), $\Theta_* = 178^\circ$ (40°), and $\gamma_{MB} = 1.0$ (0.8). Furthermore, $Q'_{10} = 10^7$ and $i_* = 85^\circ$. As $i_o \simeq 89^\circ$, the true and sky-projected misalignments are similar.

For both tidal prescriptions, the evolution of a is driven by convective damping of the equilibrium tide, which drives to orbital decay (top panels). The evolution of Ω_* is driven overall by magnetic braking if the *GN* prescription is adopted. This causes the star to spin-down. Instead, according to *Zahn*, magnetic braking dominates for the first $\simeq 2$ Gyr and the remaining evolution is driven by weak-friction tides. The latter contributes to spin-down until the system is $\simeq 5$ Gyr old and $\Theta_* > 90^\circ$. After Θ_* has crossed 90° (marked by a sudden peak in the timescales) the derivative describing the tidal evolution of the stellar spin in the weak-friction regime changes sign, and tides tend to synchronize Ω_* with Ω_o . Finally, the evolution of the misalignment is driven by IWD with the *GN* prescription and by both weak-friction tides and IWD with the *Zahn* prescription. These effects cause the misalignment to decrease to the currently observed value.

6. CONCLUSION

We investigated tidal dissipation and giant planet formation theories, by focusing on hot Jupiters with orbits close to the Roche limit (a_R). In particular, we tested whether their properties are consistent with high-eccentricity migration – where the highly eccentric orbits of giant planets are tidally circularized, through tidal dissipation in the planet, to distances larger than $2a_R$, and later orbital decay is produced by tidal dissipation

in the star. We studied CoRoT-1 b, OGLE-TR-56 b, WASP-4, 19, 48, 52, 78, and 103 b and computed the past evolution of their orbital separation, stellar spin, and misalignment (when observed), including the effects of stellar tides and wind mass loss, magnetic braking, and the evolution of the host star. For the reduction in the effectiveness of convective damping of the equilibrium tide when the forcing period is less than the turnover period of the largest eddies, we tested the linear and quadratic theory of Zahn (1966, 1989) and Goldreich & Nicholson (1977), respectively.

We found that CoRoT-1, OGLE-TR-56, WASP-48, and 103 are consistent with high-eccentricity migration, independent of the tidal prescription adopted. This same conclusion may hold for WASP-78, depending on its initial orbital configuration. This could be validated by future measurements of the transit arrival time shift (T_{shift} , e.g., Sasselov 2003; Birkby et al. 2014). Within the parameter space considered here, WASP-52 can only be explained by the *Zahn*’s (1966; 1989) prescription. Furthermore, this system could be consistent with high-eccentricity migration, depending on its initial orbital configuration. While T_{shift} for WASP-52 might be too small to detect, a more precise determination of its age could be used to distinguish between the different migration scenarios. Finally, WASP-4 and WASP-19 are consistent with high-eccentricity migration only according to *Zahn*’s (1966; 1989) prescription. For WASP-19 in particular, the fairly rapid orbital decay could lead to a significant T_{shift} which, if detected, would provide an important confirmation of these ideas.

The 3-D numerical simulations by Penev et al. (2007) showed a reduction factor that closely matched the linear prescription by Zahn (1966, 1989). With this prescription, the results presented here show that *all* systems currently known close to their Roche limit are indeed consistent with a high-eccentricity migration scenario for the formation of hot Jupiters.

This work was supported by NASA Grant NNX12AI86G. We thank Jason Steffen for his constructive remarks and comments. This research has made use of the NASA Exoplanet Archive.

REFERENCES

- Adams, E. R., López-Morales, M., Elliot, J. L., et al. 2011, *ApJ*, 741, 102
- Albrecht, S., Winn, J. N., Johnson, J. A., et al. 2012, *ApJ*, 757, 18
- Barge, P., Baglin, A., Auvergne, M., et al. 2008, *A&A*, 482, L17
- Barker, A. J., & Ogilvie, G. I. 2009, *MNRAS*, 395, 2268
- Bechter, E. B., Crepp, J. R., Ngo, H., et al. 2013, *ArXiv e-prints*, arXiv:1307.6857
- Birkby, J. L., Cappetta, M., Cruz, P., et al. 2014, *ArXiv e-prints*, arXiv:1402.5416
- Borsa, F., & Poretti, E. 2013, *MNRAS*, 428, 891
- Enoch, B., Anderson, D. R., Barros, S. C. C., et al. 2011, *AJ*, 142, 86
- Fabrycky, D., & Tremaine, S. 2007, *ApJ*, 669, 1298
- Fabrycky, D. C., & Winn, J. N. 2009, *ApJ*, 696, 1230
- Ford, E. B., & Rasio, F. A. 2006, *ApJ*, 638, L45
- Gillon, M., Smalley, B., Hebb, L., et al. 2009, *A&A*, 496, 259
- Gillon, M., Anderson, D. R., Collier-Cameron, A., et al. 2014, *ArXiv e-prints*, arXiv:1401.2784
- Goldreich, P., & Nicholson, P. D. 1977, *Icarus*, 30, 301

Table 1
Systems relevant for this work.

Name	M_{pl} (M_{J})	R_{pl} (R_{J})	M_* (M_{\odot})	R_* (R_{\odot})	$T_{\text{eff},*}$ (K)	Fe/H	$v_{\text{rot}} \sin i_*$ (km s $^{-1}$)	P_{orb} (d)	λ (deg)	i_o (deg)
C-1 ¹	1.03	1.49	$0.950^{+0.150}_{-0.150}$	$1.110^{+0.050}_{-0.050}$	6298^{+150}_{-150}	$-0.30^{+0.25}_{-0.25}$	$5.20^{+1.00}_{-1.00}$	1.509	$277.0^{+11.0}_{-11.0}$	383.80
O-56 ⁴	1.39	1.36	$1.228^{+0.072}_{-0.078}$	$1.363^{+0.089}_{-0.086}$	6050^{+100}_{-100}	$0.22^{+0.10}_{-0.10}$	$5.20^{+1.00}_{-1.00}$	1.212	—	673.72
W-4 ⁷	1.24	1.41	$0.920^{+0.060}_{-0.060}$	$0.907^{+0.014}_{-0.013}$	85500^{+100}_{-100}	$8^{-0.03+0.09}_{-0.09}$	$9.21^{+0.37}_{-0.37}$	1.338	$-1.0^{+14.0}_{-12.0}$	88.80
W-19 ¹⁰	1.11	1.40	$0.904^{+0.045}_{-0.045}$	$1.004^{+0.018}_{-0.018}$	115440^{+60}_{-60}	$12^{0.02+0.09}_{-0.09}$	$4.30^{+0.15}_{-0.15}$	0.789	$1.0^{+1.2}_{-1.2}$	78.94
W-48 ¹³	0.98	1.67	$1.190^{+0.050}_{-0.050}$	$1.750^{+0.090}_{-0.090}$	5920^{+150}_{-150}	$-0.12^{+0.12}_{-0.12}$	$3.20^{+0.30}_{-0.30}$	2.144	—	80.09
W-52 ¹⁴	0.46	1.27	$0.870^{+0.030}_{-0.030}$	$0.790^{+0.020}_{-0.020}$	5000^{+100}_{-100}	$0.03^{+0.12}_{-0.12}$	$2.50^{+1.00}_{-1.00}$	1.750	$24.0^{+17.0}_{-9.0}$	85.35
W-78 ¹⁵	0.89	1.70	$1.330^{+0.090}_{-0.090}$	$2.200^{+0.120}_{-0.120}$	6100^{+150}_{-150}	$-0.35^{+0.14}_{-0.14}$	$7.20^{+0.80}_{-0.80}$	2.175	—	83.20
W-103 ¹⁶	1.49	1.53	$1.220^{+0.039}_{-0.036}$	$1.436^{+0.052}_{-0.031}$	6110^{+160}_{-160}	$0.06^{+0.13}_{-0.13}$	$10.60^{+0.90}_{-0.90}$	0.926	—	86.30

References. — Following exoplanet.eu; (1): Barge et al. 2008; (2): Pont et al. 2010; (3): Borsa & Poretti 2013; (4): Torres et al. 2008; (5): Melo et al. 2006; (6): Adams et al. 2011; (7): Sanchis-Ojeda et al. 2011; (8): Gillon et al. 2009; (9): Triaud et al. 2010; (10): Tregloan-Reed et al. 2013; (11): Maxted et al. 2011; (12): Hebb et al. 2010; (13): Enoch et al. 2011; (14): Hébrard et al. 2013; (15): Smalley et al. 2012; (16): Gillon et al. 2014.

Note. — Observed properties of CoRoT-1 (C-1), OGLE-TR-56 (O-56), WASP-4 (W-4), WASP-19 (W-19), WAP-48 (W-48), WASP-52 (W-52), WASP-78 (W-78), and WASP-103 (W-103). The symbols are defined in § 1. The parameters listed with limited accuracy are those for which we use only the mean value.

* The rotational velocity for WASP-19 is the *true* equatorial velocity.

- Goldreich, P., & Tremaine, S. 1980, ApJ, 241, 425
Hebb, L., Collier-Cameron, A., Triaud, A. H. M. J., et al. 2010, ApJ, 708, 224
Hébrard, G., Collier Cameron, A., Brown, D. J. A., et al. 2013, A&A, 549, A134
Jackson, B., Greenberg, R., & Barnes, R. 2008, ApJ, 678, 1396
Knutson, H. A., Fulton, B. J., Montet, B. T., et al. 2013, ArXiv e-prints, arXiv:1312.2954
Lai, D. 2012, MNRAS, 423, 486
Lin, D. N. C., Bodenheimer, P., & Richardson, D. C. 1996, Nature, 380, 606
Matsumura, S., Peale, S. J., & Rasio, F. A. 2010, ApJ, 725, 1995
Maxted, P. F. L., Koen, C., & Smalley, B. 2011, MNRAS, 418, 1039
Melo, C., Santos, N. C., Pont, F., et al. 2006, A&A, 460, 251
Murray, N., Hansen, B., Holman, M., & Tremaine, S. 1998, Science, 279, 69
Nagasawa, M., Ida, S., & Bessho, T. 2008, ApJ, 678, 498
Naoz, S., Farr, W. M., Lithwick, Y., Rasio, F. A., & Teyssandier, J. 2011, Nature, 473, 187
Paczynski, B. 1971, ARA&A, 9, 183
Paxton, B., Bildsten, L., Dotter, A., et al. 2011, ApJS, 192, 3
Paxton, B., Cantiello, M., Arras, P., et al. 2013, ApJS, 208, 4
Penev, K., Sasselov, D., Robinson, F., & Demarque, P. 2007, ApJ, 655, 1166
Plavchan, P., & Bilinski, C. 2013, ApJ, 769, 86
Pont, F., Endl, M., Cochran, W. D., et al. 2010, MNRAS, 402, L1
Rasio, F. A., & Ford, E. B. 1996, Science, 274, 954
Sanchis-Ojeda, R., Winn, J. N., Holman, M. J., et al. 2011, ApJ, 733, 127
Santerne, A., Moutou, C., Barros, S. C. C., et al. 2012, A&A, 544, L12
Sasselov, D. D. 2003, ApJ, 596, 1327
Smalley, B., Anderson, D. R., Collier-Cameron, A., et al. 2012, A&A, 547, A61
Torres, G., Winn, J. N., & Holman, M. J. 2008, ApJ, 677, 1324
Tregloan-Reed, J., Southworth, J., & Tappert, C. 2013, MNRAS, 428, 3671
Triaud, A. H. M. J., Collier Cameron, A., Queloz, D., et al. 2010, A&A, 524, A25
Valsecchi, F., & Rasio, F. A. 2014, ApJ, submitted, ArXiv e-prints, arXiv:1402.3857
Ward, W. R. 1997, Icarus, 126, 261
Winn, J. N., Fabrycky, D., Albrecht, S., & Johnson, J. A. 2010, ApJ, 718, L145
Wu, Y., & Lithwick, Y. 2011, ApJ, 735, 109
Wu, Y., & Murray, N. 2003, ApJ, 589, 605
Zahn, J. P. 1966, Annales d'Astrophysique, 29, 489
Zahn, J.-P. 1989, A&A, 220, 112

Table 2
Initial a/a_R

Zahn (GN)							
Name	a_{pr} (a_R)	$t_{*,\text{lit}}$ (Gyr)	Q'_{10}	a_{in} (a_R)	$P_{\text{orb,in}}$ (days)	T_{shift} (s)	$t_{*,\text{mod}}$ (Gyr)
C-1	1.7		10^6	2.7 - 3.1 (2.0 - 2.7)	3.2 - 3.8 (2.0 - 3.2)	$\simeq 2.2 - 3.7$ (0.3 - 0.8)	4.3 - 5.1
			$\geq 10^7$	2.6 - 3.1 (2.0 - 2.7)	3.0 - 3.8 (2.0 - 3.2)	$\simeq 2.2 - 3.8$ (0.3 - 0.8)	4.3 - 5.1
O-56	1.7	1.3 ± 1	—	2.8 - 3.5 (2.2 - 2.7)	2.5 - 3.5 (1.7 - 2.3)	$\simeq 9.2 - 28$ (0.8 - 1.7)	1.3 - 3.3
W-4	1.7	$55.2^{+3.8}_{-3.2}$	<i>all</i>	2.7 - 2.9 (1.9 - 1.9)	2.6 - 3.0 ($\simeq 1.5$)	$\simeq 1.5 - 2.0$ (0.05 - 0.06)	4.9 - 6.3 ($\simeq 5.0 - 6.2$)
W-19	1.2	$611.5^{+2.8}_{-2.7}$	10^6	3.2 - 3.3 (—)	3.5 - 3.7 (—)	34 - 43 (—)	12.3 - 13.1 (—)
			10^7	3.3 (1.8 - 1.9)	3.6 (1.4 - 1.6)	36 - 38 ($\simeq 0.6 - 0.8$)	12.5 - 12.6 (12.3 - 13.3)
			10^8	3.3 (1.8)	3.7 (1.4 - 1.5)	36 ($\simeq 0.7 - 0.8$)	12.5 (12.7 - 13.3)
			10^{10}	— (1.8)	— (1.4 - 1.5)	— ($\simeq 0.7 - 0.8$)	— (12.7 - 13.3)
W-48	1.8	$27.9^{+2.0}_{-1.6}$	—	2.8 - 2.9 (2.5 - 2.6)	4.1 - 4.2 (3.4 - 3.6)	8.5 - 10 ($\sim 1.6 - 2.0$)	4.5 - 4.6
W-52	1.6	> 0.5	<i>all</i>	1.7 - 2.0 (—)	1.8 - 2.4 (—)	$\sim 0.07 - 0.2$ (—)	1.5 - 7.1 (—)
W-78	1.8	$31.37^{+1.91}_{-0.78}$	—	1.9 - 2.1	2.5 - 2.8	5.5 - 19	2.8
W-103	1.3	$4.3 - 5$	—	3.1 - 3.3 (2.4 - 3.0)	3.3 - 3.7 (2.2 - 3.1)	64 - 116 (5.2 - 7.9)	2.8 - 3.4 (2.7 - 3.4)

References. — Following exoplanet.eu; (1): Sasselov 2003; (2): Enoch et al. 2011; (3): Smalley et al. 2012 and references therein; (4): Gillon et al. 2014; (5): Gillon et al. 2009; (6): Adams et al. 2011; (7): Hébrard et al. 2013.

Note. — See Table 1 for system names. The parameter t_* is the stellar age, while T_{shift} is the transit arrival time shift (see text). The subscripts “lit” and “mod” refer to the literature and our modeling, respectively. The subscripts “in” and “pr” refer to initial (at the ZAMS) and present values, respectively. For a_{in} , $P_{\text{orb,in}}$, T_{shift} , and $t_{*,\text{mod}}$ we list outside of and in parenthesis the parameters derived using the *Zahn* and *GN* prescription for tides, respectively (§ 4). If there is no parenthesis, the two numbers agree (e.g., in W-78 the efficiency of tides is never reduced).